Spectral reflectance, transmittance, and angular scattering of materials for solar concentrators

Philipp Good [a], Thomas Cooper [a], Marco Querci [a], Nicolay Wiik [a], Gianluca Ambrosetti [b], Aldo Steinfeld [a,*]

[a] Department of Mechanical and Process Engineering, ETH Zurich, 8092 Zurich, Switzerland
[b] Airlight Energy Manufacturing SA, 6710 Biasca, Switzerland

ABSTRACT

The narrow-angle spectral specular reflectance and angular scattering of conventional and novel reflective materials for solar concentrators are measured over the wavelength range 300–2500 nm at incidence angles ranging from 15° to 60° using a spectroscopic goniometry system. The solar-weighted specular reflectance at near normal incidence and an acceptance half-angle of 17.5 mrad is 0.941 for back-silvered glass, 0.908–0.926 for silvered polymer films, 0.895 for aluminized polyester film, 0.939–0.954 for silvered aluminum sheets, and 0.860 for aluminized aluminum sheet. The angular scattering, quantified in terms of the standard deviation of a Gaussian distribution, is found to be negligible for aluminized polyester (< 0.05 mrad) and back-silvered glass (< 0.07 mrad), and noticeable for silvered polymer films (0.27–1.12 mrad) and silvered aluminum sheets (0.12–1.66 mrad). In addition, the spectral transmittance of semi-transparent materials suitable for protective covers is measured, yielding solar-weighted normal transmittance values of 0.913 and 0.946 for 100 μm thin films of ETFE (ethylene-tetrafluoroethylene) and FEP (fluorinated ethylene propylene), respectively. The measured optical properties are incorporated in a Monte Carlo ray-tracing program and applied to analyze the optical performance of solar concentrators.

© 2015 Elsevier B.V. All rights reserved.

1. Introduction

Knowledge of the optical properties of reflective materials is of paramount importance for the design of solar concentrating systems. Of interest is the reflectance weighted by the solar irradiance spectrum, which strongly affects the attainable solar concentration ratio. The spectral directional-hemispherical reflectance $R_{h,\lambda}$ at near normal incidence, with ASTM G173-03 for direct normal irradiance (DNI) at AM1.5 [1], is employed as standard for concentrating solar collectors [2]. Absolute reflectometers such as the one by NIST was developed to measure bi-directional reflectance in the range 200–2500 nm [3]. Measurements of specular reflectance were reported for several reflective materials, including back-silvered glass, metallized polymer films, and polished aluminum [4,5]. However, measured spectral data over the solar spectrum and at various incidence angles are generally not available for defined acceptance angles suited for solar applications. In addition to the reflectance, measurement of the narrow-angle surface scattering is needed for characterizing the imperfections of the solar concentrator, as these strongly influence the solar flux distributions. Surface scattering is generally understood to be a wave phenomenon of phase differences caused by surface roughness, and it is often treated as diffraction for optically smooth surfaces [6–8]. For solar concentrators, the aim is to find a convenient description of the specular reflected beam shape that can then be further applied for design purposes and performance predictions, e.g. by Monte Carlo (MC) ray-tracing. The angular scattering distribution may be accurately described by Gaussian probability density functions [4], which are straightforward to integrate into MC simulations. In addition, the standard deviation σ is a quantitative indicator of the severity of scattering and can be compared to that derived from other sources of beam spreading such as surface slope and tracking errors [4]. Reflected beam profiles of silvered polymer films applied to different substrates were measured at various incidence angles using adjustable source and detector slits combined with Fourier transform analysis [5]. More recently, angle-resolved reflectance was measured using quasi-monochromatic LEDs (455, 533, 631 nm) as light source and a CCD detector [9] and the bi-directional reflectance was measured using the principle of a Coblentz sphere [10]. In this work, we employ a spectroscopic goniometry system that enables the spectral and directional measurement of reflectance, transmittance, and scattering with high accuracy over the wide range of wavelengths and incidence angles relevant for solar concentrating applications.

* Corresponding author.
  E-mail address: aldo.steinfeld@ethz.ch (A. Steinfeld).

Nomenclature

A	illuminated area, aperture area, m^2
a	power law constant, mrad; aperture width, m
BRDF	bi-directional reflectance distribution function, sr^{-1}
C	solar concentration ratio, suns
C_g	geometric concentration ratio
d_{pixel}	pixel size, μm
F	fraction
f	focal length, m; scattering function, $mrad^{-1}$
E	direct normal irradiance, W/m^2
E_λ	spectral direct normal irradiance, $W/(m^2 \cdot nm)$
M	half-width of reference beam profile, pixel
m	discrete convolution coordinate, pixel; number of internal reflections
N	half-width of sample beam profile, pixel
n	discrete coordinate (parallel to plane of incidence), pixel; refractive index
p	power law exponent
$\hat{\mathbf{n}}$	surface normal vector
R	reflectance
$R_{specular,solar}$	solar-weighted specular reflectance
$R_{specular,\lambda}$	spectral specular reflectance
r	reference beam profile, $pixel^{-1}$; receiver radius, m; radial coordinate, m
$\hat{\mathbf{s}}$	direction vector
s	sample beam profile (reflected/transmitted), $pixel^{-1}$
T_{solar}	solar-weighted narrow-angle transmittance
T_λ	spectral narrow-angle transmittance
U	voltage, V
x	x-coordinate (parallel to plane of incidence), m
y	y-coordinate (perpendicular to plane of incidence), m
z	z-coordinate (surface normal, optical axis), m
$\eta_{optical}$	optical efficiency
θ	incidence angle, deg; zenith angle, rad; cone half-angle, mrad
λ	wavelength, nm
ρ_λ	spectral surface reflectivity
σ	standard deviation of angular scattering, mrad
τ_λ	spectral internal transmissivity
Φ	radiant flux, W
Φ_{rim}	rim angle of solar concentrator, deg
ϕ	azimuth angle, rad
χ	convolution coordinate, m
ω	solid angle, sr

Subscripts

0	front surface, surrounding medium
1	first scattering distribution; back surface, material medium
2	second scattering distribution
acc	acceptance (angle)
exp	experiment
h	directional-hemispherical (reflectance)
i	incident; inlet
n	surface slope error
o	outlet
r	reflected; radial
s	scattering (angle)
src	source (divergence angle)
t	transmitted
x	in plane of incidence
y	perpendicular to plane of incidence
λ	spectral (per unit wavelength)
$\perp$	perpendicular polarization (s)
∥	parallel polarization (p)

Abbreviations

AM	air mass
AR	anti-reflection (coating)
DNI	direct normal irradiance
FWHM	full width at half maximum
MC	Monte Carlo

In this paper, we report the spectral specular reflectance of conventional and novel solar reflective materials measured over the solar spectrum (300–2500 nm) at incidence angles ranging from 15° to 60°. The angles of source divergence (6 mrad) and detector acceptance (17.5 mrad=1°) in the plane of incidence are chosen to closely resemble the sun angle (4.65 mrad) and a typical solar receiver's acceptance angle for full interception (1°). In addition, the spectral narrow-angle transmittance of suitable semi-transparent materials for protective covers of solar concentrators is measured with the same experimental setup and characteristic angles. Furthermore, the narrow-angle surface scattering is measured over the wavelength range 350–1050 nm, which covers 75% of the DNI (ASTM G173-03 AM1.5) [1]. Finally, the measured optical properties are applied in MC ray-tracing simulations of two solar concentrators, namely a parabolic trough and a parabolic dish, to elucidate their effect on the solar flux distribution and solar concentration ratio at the focal plane, and draw conclusions for further development.

2. Materials

2.1. Reflective materials

Three types of solar reflective materials are investigated: (1) back-silvered glasses; (2) metallized polymer films; and (3) metallized aluminum sheets. An overview of the characterized materials is given in Table 1.

2.1.1. Back-silvered glass

This is a widely-used reflector material, fabricated by applying a reflective silver layer to the backside of the glass substrate by a wet chemical process and covered with a protective paint [11]. State-of-the-art parabolic trough concentrators are often constructed from 4 mm-thick back-silvered glasses. Attempts to decrease material use and cost while increasing the reflectance have triggered the development of thinner mirrors at the expense of reduced rigidity. In this study, three samples are tested with varying thickness (1–4 mm).

2.1.2. Metallized polymeric film

This lightweight alternative offers reduced material cost and weight. In this study, two samples for outdoor use are investigated: a silvered acrylic film featuring a protective copper layer at the backside, and a silvered film protected by multiple layers of semi-transparent polymers on both sides. The polymeric top layer should be highly transparent to solar radiation and resistant to abrasion and UV radiation [12]. A cost-effective alternative to silvered films are aluminized films. In contrast to silver, aluminum is highly reflective in the UV spectral range, enabling the use of inexpensive, non-UV-resistant substrate such as polyethylene

Table 1
Reflective and semi-transparent solar materials considered in this study.

Sample name	Product description	Thickness	Intended environment	Performance reported by manufacturer	
Back-silvered glass				$R_{\text{direct,solar}}$ [19]	
AgGlass4 mm	Flat glass mirror (2014)	4 mm	Outdoor	≥ 0.945 [20]	
AgGlass2 mm	Flat glass mirror (2013)	2 mm	Outdoor	≥ 0.945 [20]	
AgGlass1 mm	Flat glass mirror (2008)	1 mm	Outdoor	≥ 0.945 [20]	
Metallized polymer films				$R_{\text{h,solar}}$	$R_{\text{specular,660nm,15°,25mrad}}$
AgFilm#1	Silvered acrylic film	117 μm	Outdoor	0.94	> 0.95 [21]
AgFilm#2	Silvered polymer film	100 μm	Outdoor	0.93	0.94 [22]
AlFilm	Aluminized boPET	23 μm	Indoor	[23]	
Metallized aluminum sheets				$R_{\text{h,solar/light}}$	$R_{\text{specular, 60° ISO 7668}}$
AgSheet#1	Silvered aluminum sheet	0.5 mm	Indoor	≥ 0.95	≥ 0.92 [24]
AgSheet#2	Silvered aluminum sheet	0.4 mm	Indoor (lighting)	≥ 0.98	≥ 0.93 [25]
AgSheet#3	Silvered aluminum sheet	0.3 mm	Indoor (lighting)	≥ 0.98	≥ 0.93 [26]
AlSheet	Aluminized aluminum sheet	0.4 mm	Outdoor	≥ 0.89	≥ 0.88 [27]
Transparent polymer films					
ETFE100 μm	ETFE film	100 μm	Outdoor	[28]	
FEP100 μm	FEP film	100 μm	Outdoor	[29]	
Transparent glass				$T_{\text{normal,solar}}$	
Borosilicate3.3 mm	Borosilicate substrate	3.3 mm	Outdoor	0.92 [30]	
BorosilicateAR3.3 mm	AR-coated borosilicate	3.3 mm	Outdoor	0.97 [31]	

terephthalate (boPET) [13–15]. However, aluminized boPET requires a resistant top layer for protection from weather and abrasion.

2.1.3. Metallized aluminum sheet

Front-surface metallized aluminum offers a compromise between glass and polymer mirrors in terms of rigidity and weight/material content. Silvered aluminum sheets, originally developed for lighting applications, are interesting materials for solar concentrators, provided they are protected from weather. They comprise a pure silver layer applied onto an anodized aluminum substrate by physical vapor deposition and a reflectance enhancing dielectric layer. In this study, three samples for indoor, solar, and lighting applications are tested. For completeness, an aluminized aluminum reflector for outdoor use is also characterized. The aluminized reflector has a similar layer system as the silvered sheets, except that silver is replaced by a pure aluminum layer and a UV- and weather-resistant coating is applied on top.

2.2. Semi-transparent materials

Transparent materials are used to protect reflectors [16,17]. A lightweight alternative to glass are semi-transparent polymeric films [13–15], such as ethylene-tetrafluoroethylene (ETFE) and fluorinated ethylene propylene (FEP) because of their favorable optical, chemical, and mechanical properties [18]. The spectral narrow-angle transmittance of 100 μm thin films of ETFE and FEP is measured. For comparison, the narrow-angle transmittance spectra of a borosilicate substrate and an anti-reflection (AR) coated borosilicate are also measured.

3. Reflectance and transmittance

The spectral specular reflectance $R_{\text{specular},\lambda}$ at a certain incidence angle θ and azimuth angle ϕ is defined as the fraction of spectral radiant flux incident on a surface element dA from a solid angle ω_{src} that is reflected in the specular direction within a solid angle ω_{acc}. Assuming that the incident radiance on the sample is uniform and isotropic within ω_{src}, this may be expressed as a bi-conical reflectance using the bi-directional reflectance distribution
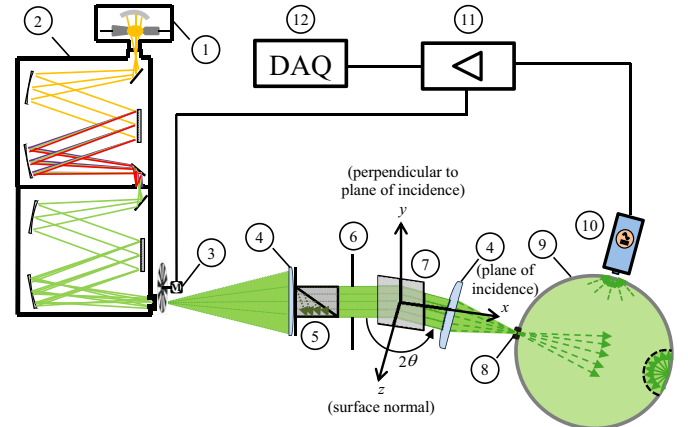

Fig. 1. The spectroscopic goniometry system comprised of: (1) Xe-arc lamp, (2) double monochromator, (3) chopper, (4) imaging lens pair, (5) polarizer, (6) iris, (7) sample, (8) mechanical slit, (9) integrating sphere, (10) photodetector, (11) lock-in amplifier, and (12) data acquisition system. The x–y–z coordinate system is centered at the pivot point and x–z defines the plane of incidence.

function (BRDF) of the surface [32]:

$$R_{\text{specular},\lambda}(\lambda, \theta, \phi, \omega_{\text{src}}, \omega_{\text{acc}}) \equiv \frac{d\Phi_{r,\lambda}(\lambda, \theta, \phi, \omega_{\text{acc}})}{d\Phi_{i,\lambda}(\lambda, \theta, \phi, \omega_{\text{src}})}$$

$$= \frac{\int_{\omega_{\text{acc}}} \int_{\omega_{\text{src}}} \text{BRDF}(\lambda, \theta_i, \phi_i, \theta_r, \phi_r) \cos\theta_i d\omega_i \cos\theta_r d\omega_r}{\int_{\omega_{\text{src}}} \cos\theta_i d\omega_i} \quad (1)$$

Here the reflectance is denoted by R to indicate that solar reflective materials usually consist of several layers and thus the measured reflectance is an overall extensive property resulting from multiple interactions of light with optical interfaces rather than an intensive property such as the reflectivity ρ of a single surface. The solar-weighted specular reflectance is given by:

$$R_{\text{specular,solar}} = \frac{\int R_{\text{specular},\lambda} E_\lambda d\lambda}{E} \quad (2)$$

where E_λ and E are the spectral and total direct normal solar irradiance, respectively (ASTM G173-03 AM1.5). Numerical integration is performed over the spectral range 300–2500 nm using the weighed ordinate method [33]. The spectral narrow-angle transmittance T_λ is defined as the fraction of spectral radiant flux
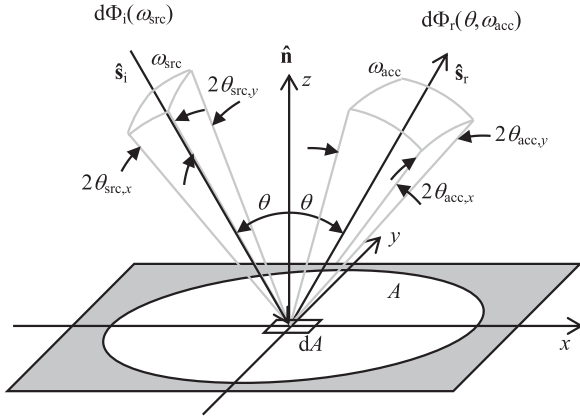
$\mathrm{d}\Phi_i(\omega_{\mathrm{src}})$ $\mathrm{d}\Phi_r(\theta, \omega_{\mathrm{acc}})$

Fig. 2. Geometry of incident and specular reflected beams on a flat surface.

incident from a solid angle ω_{src} on a surface element $\mathrm{d}A$ of a semi-transparent medium layer that is transmitted and leaves the medium along the incident direction within a solid angle ω_{acc},

$$T_\lambda(\lambda, \theta, \phi, \omega_{\mathrm{src}}, \omega_{\mathrm{acc}}) \equiv \frac{\mathrm{d}\Phi_{\mathrm{t},\lambda}(\lambda, \theta, \phi, \omega_{\mathrm{acc}})}{\mathrm{d}\Phi_{\mathrm{i},\lambda}(\lambda, \theta, \phi, \omega_{\mathrm{src}})} \qquad (3)$$

For a smooth single-layered non-scattering semi-transparent medium, the spectral transmittance T_λ is given in terms of its surface's spectral reflectivity ρ_λ and medium's spectral transmissivity τ_λ [34]:

$$T_\lambda = \frac{\tau_\lambda(1-\rho_\lambda)^2}{1-\rho_\lambda^2\tau_\lambda^2} \qquad (4)$$

The solar-weighted narrow-angle transmittance is given by:

$$T_{\mathrm{solar}} = \frac{\int T_\lambda E_\lambda \mathrm{d}\lambda}{E} \qquad (5)$$

3.1. Experimental setup

Measurements are performed using a spectroscopic goniometry system [35], shown schematically in Fig. 1. A xenon-arc lamp (rated input power: 150 W) is used as light source (1). An aspherical Czerny-Turner type double monochromator (2) enables spectral measurements in the range 300–2500 nm with a full bandwidth at half maximum (FWHM) 15–30 nm. A mechanical beam chopper (3) modulates the nearly monochromatic light at a frequency of 417 Hz. The diverging light beam is collimated by a MgF$_2$ plano-convex lens (4). A calcite Glan–Thompson polarizer (5) is inserted after the collimating lens for materials showing polarization-dependent optical properties. The last component on the source side is an iris (6) with adjustable size acting as the aperture stop. On the detector side, the light beam is focused by a second MgF$_2$ plano-convex lens (4) to an adjustable mechanical slit (8). With this arrangement, the monochromator exit slit is imaged onto the mechanical slit which acts as the field stop and allows to precisely adjust the desired acceptance angle of the detector. The light passing through is then collected in an integrating sphere (diameter: 50 mm) (9). The diffused light is measured at the detector port by a thermoelectrically cooled Si or PbS photodiode detector (10), depending on the wavelength (Si: 300–1000 nm, PbS: 1000–2800 nm). The detected photocurrent is further converted to a proportional voltage by a transimpedance amplifier. To compensate for changes in focal length due to spectral dispersion, the axial locations of the lenses are automatically adjusted by linear translation stages. In the spectral region 500–1000 nm where the Xe-arc lamp reaches its maximum emissive power, neutral density filters are placed in front of the second lens to prevent detector

overloading. All components of the detector side are mounted on a rotatable arm that can be moved to angular positions ranging from 30° to 180° as measured from the source beam direction (cf. Fig. 1). This imposes a lower limit on the minimum incidence angle for measuring reflectance of 15°. The sample (7) is mounted on a rotatable base plate that allows adjusting the desired incidence angle. Different sample holders are used for rigid and flexible materials. For rigid materials such as back-silvered glasses and aluminum sheets, the samples are softly clamped at their bottom edge. In this case, the maximum measurable incidence angle is only constrained by the samples size and is usually greater than 75°. Samples of flexible polymer films are fixed in a custom-made sample holder that allows for slight tensioning to create a flat surface. The maximum measurable incidence angle is then limited by the frame size to below 65°. The whole sample assembly is mounted on a three-axis linear translation table that allows for automatic adjustment of the sample position. For the reflectance measurement, the sample is always aligned such that the reflective surface passes through the pivot point of the rotatable detector arm. The lock-in amplifier (11) is frequency-synchronized with the chopper to measure the pulsed signal, thereby minimizing noise from other sources.

When compared to conventional circular-aperture measurements, slit-aperture measurements features two-fold advantages: it enables measurement of the specular reflectance and angular scattering in different directions and thus detection of anisotropic behavior [4]; and it uses only two lenses which reduces misalignment. Standard values for the source beam divergence (θ_{src}) and detector acceptance (θ_{acc}) angles for specular reflectance measurements of anodized aluminum surfaces are given in Ref. [36]. In the plane of incidence, the standard source half-angle is $0.375° = 6.5$ mrad, whereas the standard acceptance half-angle varies from $0.9° = 15.7$ mrad at $\theta = 20°$ to $2.2° = 38.4$ mrad at $\theta = 60°$ [36]. In the present study, the source divergence half-angle in the plane of incidence is set to $\theta_{\mathrm{src},x} = 6$ mrad, which includes roughly 97% of the direct normal and circumsolar irradiance assuming the standard solar scan sunshape [37]. The acceptance half-angle is set to $\theta_{\mathrm{acc},x} = 17.5$ mrad $= 1°$ at all incidence angles. This choice of angles closely matches the operating conditions of reflective materials for solar concentrators. In the plane perpendicular to the plane of incidence, the acceptance angle ($\theta_{\mathrm{acc},y} = 50$ mrad) is chosen roughly 6 times larger than the source divergence angle ($\theta_{\mathrm{src},y} = 8$ mrad), similar to [4]. To compensate for the change in lens focal length at different wavelengths, the position of each lens in the imaging lens pair is automatically adjusted by a linear translation stage. The resulting maximum deviations of the source beam and detector acceptance angles occur at the minimum (300 nm) and maximum (2500 nm) measured wavelengths and are within the standard tolerances [36]. The geometry of the incident and specular reflected beams is shown in Fig. 2.

3.2. Methods

For each data point of $R_{\mathrm{specular},\lambda}$, three sequential measurements are performed at the same wavelength λ: (1) a reference measurement of incident radiative flux with the detector arm located at 180° and the sample moved out of the beam; (2) a sample measurement of reflected radiative flux with the reflective sample placed in the source beam at an incidence angle θ and the detector arm rotated to 2θ; and (3) a second reference measurement of incident flux to account for temporal fluctuations in Xe-arc lamp power, since a single-beam setup is used. The $R_{\mathrm{specular},\lambda}$ is then calculated as the ratio of the voltage from the sample measurement to the average voltage from the reference measurements, assuming that the measured voltage U is proportional to the
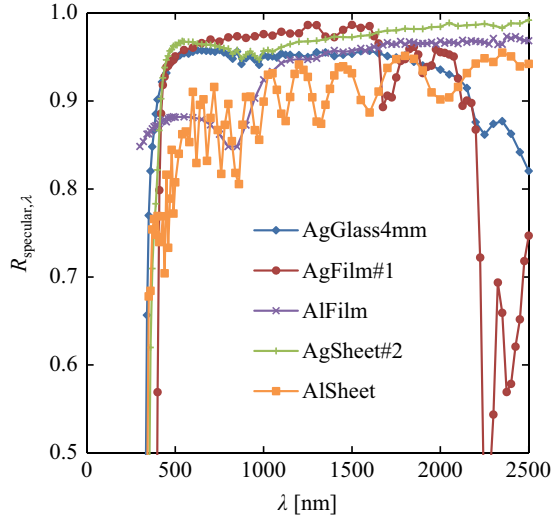
Fig. 3. Spectral specular reflectance at $\theta = 15°$ and $\theta_{acc,x} = 17.5$ mrad of back-silvered glass, silvered and aluminized polymer films, and silvered and aluminized aluminum sheets.

radiant flux:

$$R_{specular,\lambda}(\lambda, \theta) \equiv \frac{\Phi_{r,\lambda}(\lambda, \theta)}{\Phi_{i,\lambda}(\lambda)} = \frac{U_{sample}(\lambda, \theta)}{U_{reference}(\lambda)} \qquad (6)$$

It is noted that the measurement is absolute in nature as the final result does not depend on any calibrated reference material. If the optical property of interest depends on the state of polarization of the incident light, the above measurement is performed twice, with the electric field of incident light oscillating once in the plane parallel to the plane of incidence (parallel ($\parallel$) or p-polarized), and once in the plane perpendicular to the plane of incidence (perpendicularly ($\perp$) or s-polarized). The optical property for unpolarized sunlight is then calculated as the average of p- and s-polarized reflectance [38]

$$R_{specular,\lambda} = \frac{1}{2}(R_{specular,\lambda,\parallel} + R_{specular,\lambda,\perp}) \qquad (7)$$

For measurement of T_λ, the exact same procedure is applied with the only difference to the reflectance measurement being that the detector arm remains at 180° also during the sample measurement.

3.3. Results and discussion

3.3.1. Specular reflectance

The measured specular reflectance spectra at near normal incidence (15°) of five samples of the solar reflective materials (listed in Table 1) are shown in Fig. 3. $R_{specular,solar}$ for all characterized materials at all incidence angles are listed in Table 2. The spectral data measured at all incidence angles are available in Ref [39]. While the spectral differences among the reflective materials are substantial, the dependence of specular reflectance on the incidence angle is generally weak. The maximum change in $R_{specular,solar}$ between 15° and 60° is within 1.5% for all tested materials.

3.3.1.1. Back-silvered glass.
The measured $R_{specular,solar}$ of AgGlass4 mm at $\theta = 15°$ (0.941) is close to the solar direct reflectance [19] at near normal incidence stated by the manufacturer (≥ 0.945) [20]. Theoretically, the reflectance should increase with decreasing glass thickness due to reduced absorption in the glass layer, as observed for AgGlass2 mm. The somewhat lower

Table 2
Solar-weighted narrow-angle transmittance of semi-transparent materials and solar-weighted specular reflectance of reflective materials as a function of incidence angle.

| T_{solar}	0°	15°	45°	60°
ETFE100 μm	0.913	0.910	0.889	0.831
FEP100 μm	0.946	0.944	0.932	0.877
Borosilicate3.3 mm	0.921			
BorosilicateAR3.3 mm	0.950	0.949	0.940	0.880
$R_{specular,solar}$		15°	45°	60°
AgGlass4 mm (2014)		0.942	0.935	0.934
AgGlass2 mm (2013)			0.941	
AgGlass1 mm (2008)			0.934	
AgFilm#1		0.926	0.922	0.913
AgFilm#2		0.908	0.901	0.893
AlFilm		0.895	0.898	0.894
AgSheet#1		0.939	0.941	0.944
AgSheet#2		0.948	0.949	0.949
AgSheet#3		0.954	0.951	0.952
AlSheet		0.860	0.865	
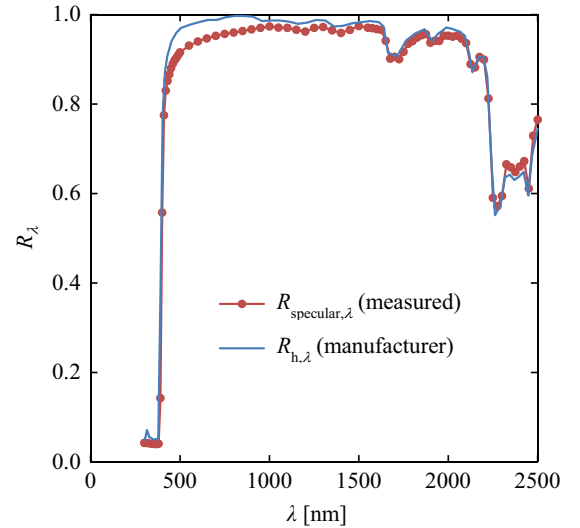
Fig. 4. AgFilm#2: spectral specular reflectance measured at $\theta = 15°$ and $\theta_{acc,x} = 17.5$ mrad and spectral directional-hemispherical reflectance given by the manufacturer [22].

performance of AgGlass1 mm is attributed to the age of that sample and improvements in the fabrication process over time.

3.3.1.2. Metallized polymer films.
For the AgFilms#1 and #2, the solar-weighted directional-hemispherical reflectance $R_{h,solar}$ stated by the manufacturer is 1.4% and 2.2% higher than the measured $R_{specular,solar}$ at 15°, respectively (cf. Tables 1 and 2). The spectra of $R_{h,\lambda}$ provided by the manufacturer [22] and $R_{specular,\lambda}$ measured at 15° incidence angle are shown in Fig. 4 for AgFilm#2. A significant difference, e.g. 5.5% at 500 nm, is observed especially in the visible range where the solar irradiance peaks. The difference decreases towards longer wavelengths until specular and hemispherical reflectance become identical beyond 2000 nm. A higher specular than hemispherical reflectance above 2250 nm is attributed to increased measurement uncertainty at longer wavelengths. Interestingly, AgFilm#2 and AlFilm feature comparable $R_{specular,solar}$, although the latter is cheaper. Note that aluminized boPET has no protective top layer but it is restricted to applications in a protected environment.
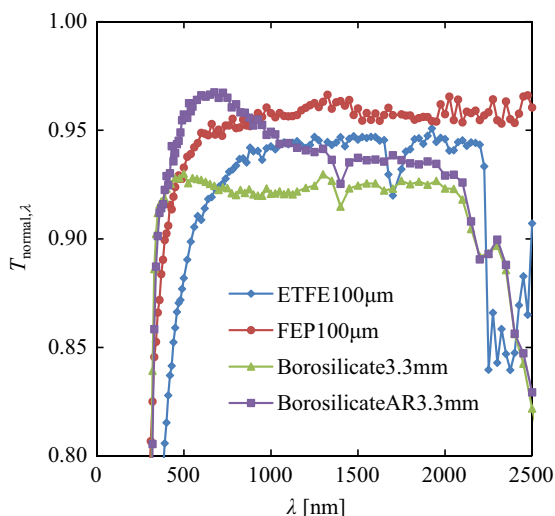
Fig. 5. Spectral normal transmittance at $\theta_{acc,x} = 17.5$ mrad of semi-transparent polymeric films and borosilicate glasses.

Fig. 6. Experimental setup for angular scattering measurements comprised of: (1) Xe-arc lamp, (2) double monochromator, (3) imaging lens pair, (4) iris, (5) sample, (6) CCD detector, (7) data acquisition system, (8) 2D grayscale image, and (9) normalized, averaged 1D beam profile.

3.3.1.3. Metallized aluminum sheets. The measured $R_{specular,solar}$ of silvered aluminum sheets lies between the specular and directional-hemispherical reflectance stated by the manufacturers [24–26] for solar radiation (AgSheet#1) or visible light (AgSheet#2 and #3). Reflectors for lighting (#2 and #3) generally show a higher $R_{specular,solar}$ than that for solar applications (#1), but other factors such as durability and weather resistance should be taken into account for the selection of appropriate materials. The aluminized reflector for outdoor use shows interference patterns (cf. Fig. 3) caused by the protective, weather resistant, transparent top coating. In addition, $R_{specular,solar}$ determined in this study for AlSheet is clearly lower than $R_{h,solar}$ (≥ 0.89) and $R_{specular,ISO\ 7668\ 60°}$ (≥ 0.88) stated by the manufacturer [27]. A reason for this is the difference in acceptance angles used in this work (1°) and defined in ISO 7668 (2.2°), combined with significant angular scattering by the reflective surface. At 45° incidence angle and 550 nm, the relative difference between $R_{specular,\lambda}$ measured with acceptance angles of 2.2° and 1° in the plane of incidence is 1.0% and decreases with increasing wavelength. Furthermore, $R_{specular,\lambda}$ of AgSheet#2 and AlSheet was measured with the rolling marks of the aluminum substrate perpendicular to the plane of incidence, which yields $R_{specular,solar}$ that is roughly 0.5% lower than when measured with the rolling marks parallel to the plane of incidence.

3.3.2. Narrow-angle transmittance

The measured spectral normal transmittance $T_{normal,\lambda}$ of the 100 µm ETFE and FEP films and the 3.3 mm borosilicate glasses (substrate and AR-coated) is shown in Fig. 5. The spectral data at all incidence angles are available in [39]. Fluctuations at longer wavelength is attributed to thin-film interference. T_{solar} at different incidence angles are also given in Table 2. While the 100 µm ETFE film shows a comparable value of T_{solar} as that for a 3.3 mm borosilicate glass, the 100 µm FEP film is almost as transparent as the AR-coated borosilicate glass.

4. Angle-resolved surface scattering

The narrow-angle scattering of reflective materials within the acceptance solid angle for specular reflectance is determined using a combined experimental-numerical approach. First, the shapes of the reference and specular reflected beams are measured. Then the scattering function is determined by a deconvolution of the i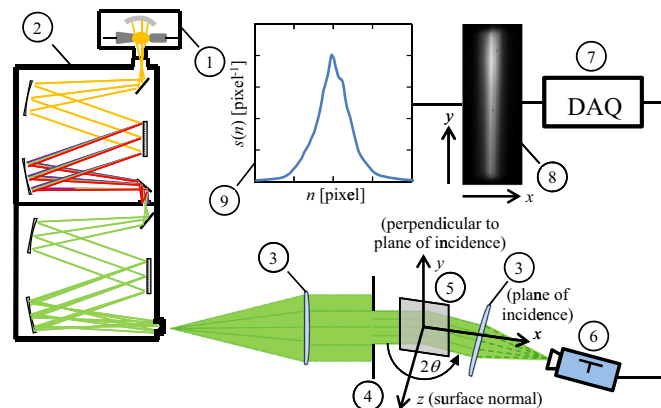ncident beam from the reflected beam. Finally, the angular scattering is quantified by parameter estimation of statistical scattering models using the least-square method.

4.1. Experimental setup

The modified experimental setup for the beam shape measurements is shown in Fig. 6. On the source side, the monochromator exit slit width is reduced to achieve a highly collimated beam in the plane of incidence ($\theta_{src,x} = 0.31$ mrad), while the chopper is removed. On the detector side, the $f_{acc} = 75$ mm lens is replaced by a $f_{acc} = 250$ mm lens to refine the angular resolution of the setup. Most importantly, the detector assembly (adjustable slit + integrating sphere + photodetector) is replaced by an area scan CCD camera (Basler scA780–54 gm, resolution: 782×582, pixel size: 8.3 µm $\times$ 8.3 µm, frame rate: 55 fps) with the sensor area placed at the rear focal point of the second lens. The CCD detector enables measurements in the spectral range 350–1050 nm, which includes 75% of ASTM G173-03 AM1.5 reference spectrum for DNI.

The measurement procedure is similar to that described in the previous section. For every angular scattering experiment, three images are recorded at the same wavelength: (1) reference beam measurement with the sample moved out of the beam and the detector arm positioned at 180° such that the image of the monochromator exit slit is projected at the CCD detector; (2) reflected/transmitted beam shape measurement with the sample moved into the path of light at an angle θ and the detector arm rotated to the corresponding angular position (2θ for reflection; 180° for transmission); and (3) a second reference beam measurement. The exposure time is adjusted for every experiment such that no saturation is detected in the recorded images. With the slit aperture setup, the scattering in the plane of incidence (x-direction) may be observed in each slit cross-section along the y-direction. This allows for averaging over y and extracting a 1D beam profile as a function of x. For this purpose, the 1D beam profiles at each slit cross-section in y are normalized for a unity area below the curve. The normalized 1D beam profiles are then averaged over a certain y-range to obtain a representative average beam profile. This measurement procedure defines a controlled experiment with high repeatability. For anisotropic materials that show visible marks originating from the fabrication of the substrate (e.g. sheet rolling, film extrusion), the measurement is performed once with the manufacturing marks parallel and once perpendicular to the plane of incidence.

Table 3
Best fit standard deviations of single Gaussian angular scattering distribution as a function of wavelength and incidence angle for all tested materials and manufacturing direction orientations.

Material	λ [nm] θ [deg]	350	400	500	555	600 σ [mrad]	700	800	950	1050
ETFE100 μm	0–60	< 0.033								< 0.033
FEP100 μm	0–45	< 0.033								< 0.033
	60	0.049	0.049	0.044	0.041	0.038	0.037	0.039	0.033	0.033
AlFilm	15–45	< 0.033								< 0.033
	60	0.042	0.048	0.042	0.038	0.042	0.040	0.038	0.036	0.039
AgGlass4 mm	15	< 0.033	0.036	< 0.033						< 0.033
	45	0.040	0.043	0.041	0.038	< 0.033	0.036	0.035	< 0.033	< 0.033
	60	0.060	0.064	0.057	0.055	0.053	0.053	0.058	0.053	0.049
AgFilm#1	15		0.34	0.33	0.33	0.32	0.31	0.31	0.30	0.29
Marks parallel to	45		0.39	0.38	0.37	0.37	0.36	0.35	0.35	0.34
Plane of incidence	60		0.49	0.50	0.50	0.50	0.49	0.48	0.46	0.47
AgFilm#1	15		0.76	0.70	0.70	0.68	0.62	0.60	0.55	0.58
marks perp. to	45		0.86	0.82	0.78	0.76	0.73	0.67	0.63	0.56
Plane of incidence	60		1.01	0.99	0.93	0.93	0.90	0.80	0.71	0.76
AgFilm#2	15		0.65	0.59	0.57	0.55	0.50	0.46	0.40	0.35
Marks parallel to	45		0.69	0.62	0.58	0.55	0.47	0.43	0.34	0.30
Plane of incidence	60		0.71	0.62	0.56	0.51	0.42	0.37	0.29	0.27
AgFilm#2	15		0.72	0.66	0.64	0.62	0.56	0.52	0.47	0.45
Marks perp. to	45		0.86	0.77	0.71	0.68	0.61	0.60	0.48	0.46
Plane of incidence	60		1.12	0.98	0.93	0.88	0.77	0.85	0.71	0.55
AgSheet#1	15	0.58	0.56	0.55	0.55	0.54	0.53	0.52	0.51	0.51
Marks parallel to	45	0.67	0.66	0.65	0.65	0.65	0.63	0.63	0.62	0.61
Plane of incidence	60	0.83	0.82	0.82	0.82	0.81	0.80	0.80	0.80	0.79
AgSheet#1	15	0.40	0.37	0.31	0.29	0.27	0.23	0.21	0.18	0.16
Marks perp. to	45	0.33	0.29	0.24	0.22	0.21	0.19	0.17	0.15	0.13
Plane of incidence	60	0.27	0.24	0.21	0.20	0.19	0.16	0.15	0.14	0.12
AgSheet#2	15	1.04	1.03	1.01	1.00	1.00	0.99	0.99	0.98	0.97
Marks parallel to	45	1.28	1.27	1.25	1.24	1.25	1.24	1.25	1.24	1.23
Plane of incidence	60	1.66	1.66	1.64	1.64	1.65	1.64	1.66	1.66	1.65
AgSheet#2	15	0.38	0.34	0.28	0.26	0.24	0.22	0.20	0.18	0.17
Marks perp. to	45	0.33	0.31	0.27	0.26	0.25	0.24	0.23	0.21	0.21
Plane of incidence	60	0.32	0.31	0.29	0.28	0.28	0.27	0.27	0.26	0.26

4.2. Methods

4.2.1. Deconvolution

The sample beam profile $s(x)$ is a convolution of the reference beam profile $r(x)$ with the scattering function $f(x)$ of the material [4],

$$s(x) = (r * f)(x) = \int_{-\infty}^{\infty} r(\chi)f(x-\chi)\mathrm{d}\chi \tag{8}$$

Due to the finite resolution of the CCD sensor, the measured beam profiles are discrete functions $r(n)$ and $s(n)$ related by a discrete convolution. Since the beam profiles are finite, i.e. $r(n)=0$ for $|n| > M$ and $s(n)=0$ for $|n| > N$, and thus $f(n)=0$ for $|n| > N - M$, the equations for the $2N+1$ non-zero elements of $s(n)$ are given by,

$$s(n) = \sum_{m = n-(N-M)}^{n+N-M} r(m)f(n-m), \quad \text{for } -N \le n \le N \tag{9}$$

This yields $2N+1$ linear equations for the $2(N-M)+1$ unknown non-zero elements of $f(n)$. The discrete scattering function can be determined by solving a linear least-square optimization problem. If needed, filtering can be applied a *posteriori* to obtain a smooth curve. For smoothing a scattering function, a non-causal weighted moving average filter is recommended since it does not introduce any phase delay. Finally, the imaging equation is applied to transform from pixel coordinates to scattering angle $\theta_{s,x}$:

$$\theta_{s,x} = \arctan\left(\frac{n \cdot d_{\text{pixel}}}{2f_{\text{acc}}}\right) \approx \frac{n \cdot d_{\text{pixel}}}{2f_{\text{acc}}} \tag{10}$$

where $d_{\text{pixel}}=8.3$ μm is the pixel size of the CCD detector and $f_{\text{acc}}=250$ mm the focal length of the lens on the detector side. The profiles of the reference and sample beams are normalized for a unity area below the curve. Thus, the integral of the scattering function is 1 and $f(\theta_{s,x})$ becomes the probability density function of the scattering angle. The discrete deconvolution method provides an independent result for the scattering function without imposing any assumptions about its shape. However, for comparison among materials, a description based on a few characteristic parameters rather than a complete curve would be more convenient. Such a description is obtained by assuming a certain statistical scattering distribution model and identifying the best fitting parameters.

4.2.2. Statistical surface scattering models

It is generally assumed that surface scattering of solar reflective materials may be described by a scattering angle following a Gaussian distribution with zero mean and standard deviation σ [4,40],

$$f(\theta_{s,x}) = \frac{1}{\sqrt{2\pi\sigma^2}}\exp\left(-\frac{\theta_{s,x}^2}{2\sigma^2}\right) \tag{11}$$

or by a superposition of two Gaussian distributions for materials that show different light scattering mechanisms, e.g. due to microscopic and macroscopic surface roughness of the reflective layer and the substrate, respectively [4]

$$f(\theta_{s,x}) = \frac{F_1}{\sqrt{2\pi\sigma_1^2}}\exp\left(-\frac{\theta_{s,x}^2}{2\sigma_1^2}\right) + \frac{1-F_1}{\sqrt{2\pi\sigma_2^2}}\exp\left(-\frac{\theta_{s,x}^2}{2\sigma_2^2}\right) \tag{12}$$

Using the experimentally measured reference beam profile and a Gaussian model for the scattering function, the scattered beam profile predicted by the model s_{model} is calculated according to Eq. (9). The standard deviations are determined by minimizing the deviations from the experimentally measured sample beam profile
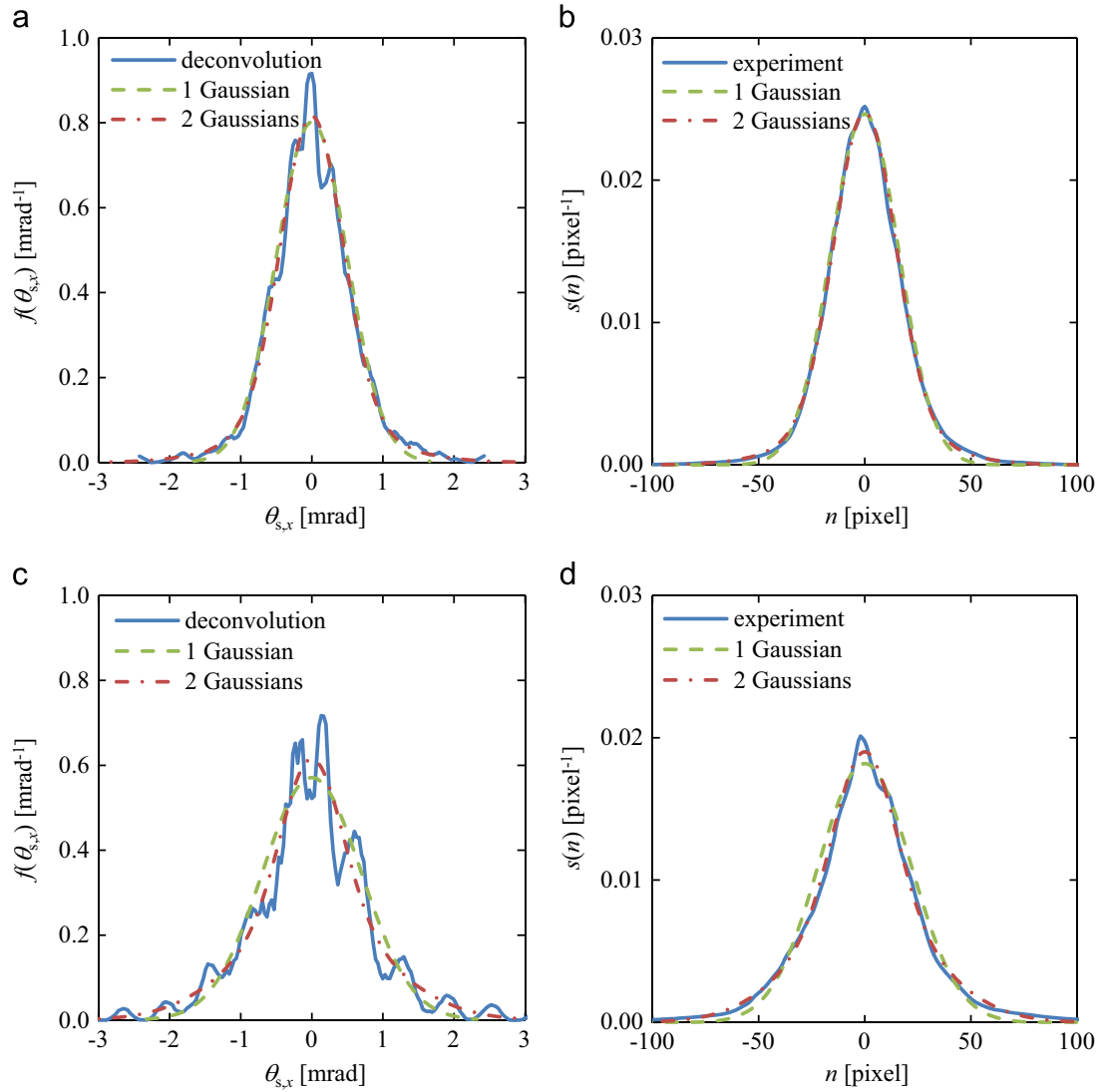
Fig. 7. AgFilm#1 with manufacturing marks parallel to plane of incidence at $\theta=60°$ (a,b); and perpendicular to plane of incidence at $\theta=15°$ (c,d). (a/c) Deconvolved, and best fit single and double Gaussian scattering functions; and (b/d) reflected beam profiles measured experimentally, and modeled with the single and double Gaussian scattering functions at 555 nm.

s_{exp},

$$\min_{\sigma} \sum_{n=-N}^{N} \left(s_{model}(n) - s_{exp}(n) \right)^2 \tag{13}$$

For anisotropic materials, the 1D scattering functions identified from the beam shape measurements in the two main directions of the material are finally combined to a 2D scattering function. Assuming orthotropic and independent scattering in the two main directions, the 2D scattering distribution function is the product of the 1D scattering functions in each direction. For single Gaussian distributions in both directions, this yields a bivariate Gaussian distribution:

$$f(\theta_{s,x}, \theta_{s,y}) = f(\theta_{s,x})f(\theta_{s,y})$$
$$= \frac{1}{2\pi\sigma_x\sigma_y} \exp\left(-\frac{\theta_{s,x}^2}{2\sigma_x^2} - \frac{\theta_{s,y}^2}{2\sigma_y^2} \right) \tag{14}$$

4.3. Results

Angular scattering experiments are performed for the reflective materials AgGlass 4 mm, AgFilm#1 and #2, AlFilm, and AgSheet#1

and #2, and for the semi-transparent films ETFE100 µm and FEP100 µm. The estimated standard deviations of the best fit Gaussian scattering distribution as a function of wavelength and incidence angle for all tested materials are summarized in Table 3.

4.3.1. Highly specular materials

Very small angular scattering is measured for reflection from back-silvered glass and aluminized boPET, and for transmission through semi-transparent polymer films. The angular scattering of these materials is accurately described by a single Gaussian distribution according to Eq. (11), with standard deviations < 0.03 mrad for ETFE100 µm, < 0.05 mrad for FEP100 µm, < 0.05 mrad for AlFilm, and < 0.07 mrad for AgGlass4 mm at all measured wavelengths and incidence angles. It is noted that these values are in the range of the angular resolution of the experimental setup (0.033 mrad) and are thus subject to inaccuracies evolving from discrete sampling of the beam profiles. Standard deviations below the angular resolution of the setup are reported as < 0.033 mrad in Table 3.

4.3.2. Silvered polymeric films

Significant light scattering is observed for reflection from silvered polymers. Fig. 7a) shows the scattering functions obtained by
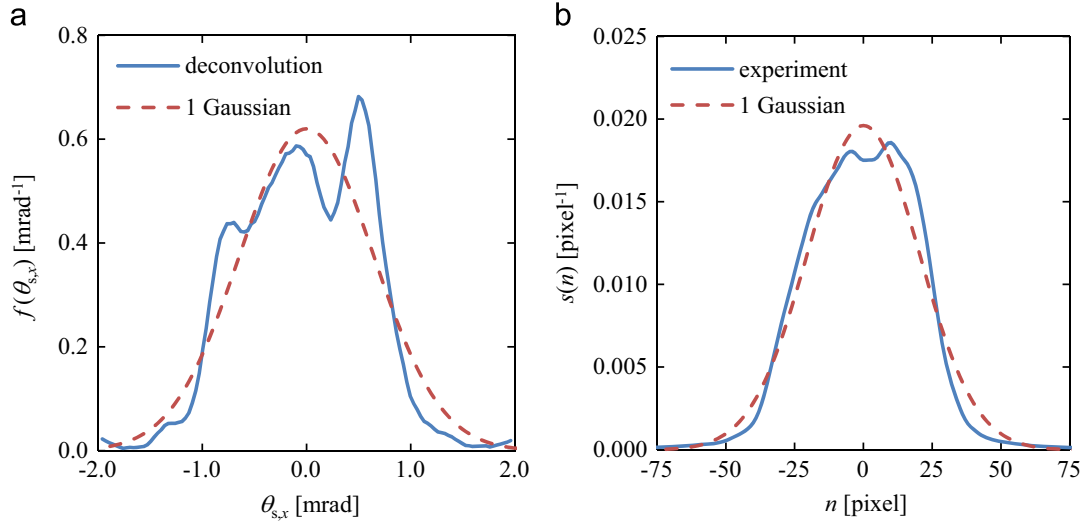
Fig. 8. AgSheet#1 with manufacturing marks oriented parallel to the plane of incidence at $\theta=45°$ and 555 nm. (a) Deconvolved and best fit single Gaussian scattering functions; and (b) reflected beam profiles measured experimentally, and modeled with the single Gaussian scattering function.
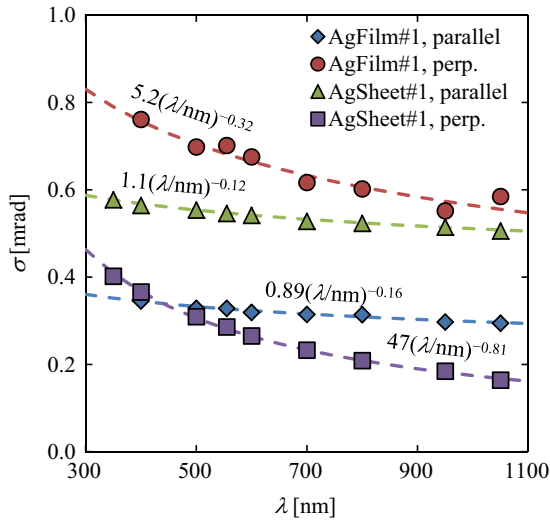

Fig. 9. AgFilm#1 and AgSheet#1 in the two main directions at $\theta=15°$. Standard deviation of angular scattering as a function of wavelength (markers) and power laws for the different series (dashed lines).

deconvolution and by least-square fitting of a single Gaussian and a superposition of two Gaussian distributions for the AgFilm#1 with the manufacturing marks parallel to the plane of incidence. The best fits to the experimentally measured reflected beam profile are shown in Fig. 7b). The single Gaussian distribution shows a good agreement in the central region of the reflected beam profile only, whereas the superposition of two Gaussian distributions according to Eq. (12) resolves also the tail regions. The best fit parameters of the double Gaussian distribution are summarized in Ref. [39] for all measured wavelengths and incidence angles. The scattering functions and reflected beam profiles for AgFilm#1 with the manufacturing direction perpendicular to the plane of incidence are shown in Fig. 7c) and d), respectively. In this direction the scatter is generally larger than when aligned with the marks parallel to the plane of incidence. Furthermore, the deconvolved scattering function indicates a presence of diffraction peaks, which cannot be captured by a Gaussian distribution. Nevertheless, the reflected beam profile is still reproduced with reasonable accuracy by a superposition of two Gaussian distributions.

4.3.3. Silvered aluminum sheets

Similar to silvered polymer films (cf. Fig. 7), the scattering of silvered aluminum sheets with the rolling marks of the aluminum substrate perpendicular to the plane of incidence is accurately described by a superposition of two Gaussian distributions. However, the silvered sheets are highly anisotropic. The deconvolved and best fit Gaussian scattering functions and the experimentally measured and statistically modeled reflected beam profiles of the AgSheet#1 with the rolling marks parallel to the plane of incidence are shown in Fig. 8a) and b), respectively. For modeling such a beam shape, the superposition of two Gaussian distributions shows no benefit and is thus not shown in the figure. Due to the noticeable deviation between the experimentally measured and statistically modeled beam profiles it might be worth the effort to use the deconvolved scattering function rather than a Gaussian distribution for accurate simulations.

4.4. Discussion

4.4.1. Wavelength dependence

The standard deviations from Table 3 for AgFilm#1 and AgSheet#1 with the marks parallel and perpendicular to the plane of incidence at 15° incidence angle are plotted as a function of wavelength in Fig. 9. The standard deviation of the scattering distribution is generally decreasing at longer wavelength for all tested materials at all incidence angles. This is consistent with the theory of light scattering for smooth surfaces that predicts an inversely proportional relationship between scatter distribution width and wavelength [7,41]. An empirical fit to the measured data points is obtained by a power law of the form $\sigma = a \cdot (\lambda/\mathrm{nm})^p$. The trend lines and best fit equations are also shown in Fig. 9. The good agreement between the measured data and the power laws allows for interpolation and – to some extent – for certain extrapolation outside the measured range.

4.4.2. Incidence angle dependence

The standard deviation of the scattering distribution as a function of incidence angle at a wavelength of 555 nm is shown in Fig. 10 for the same materials and same manufacturing directions as in Fig. 9. The scatter generally increases with increasing incidence angle for all tested materials except for the silvered aluminum sheets #1 and #2 with the rolling marks perpendicular to the plane of incidence. The scattering theory for smooth surfaces predicts a shift invariant scattering function in direction cosine
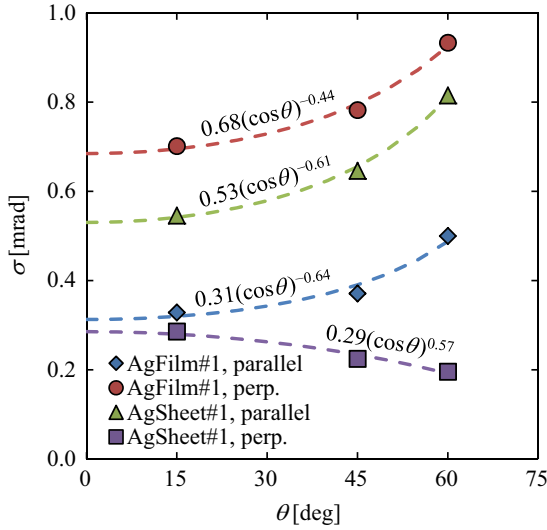
Fig. 10. AgFilm#1 and AgSheet#1 in the two main directions at 555 nm. Standard deviation of angular scattering as a function of incidence angle (markers) and power laws in $\cos\theta$ (dashed lines).
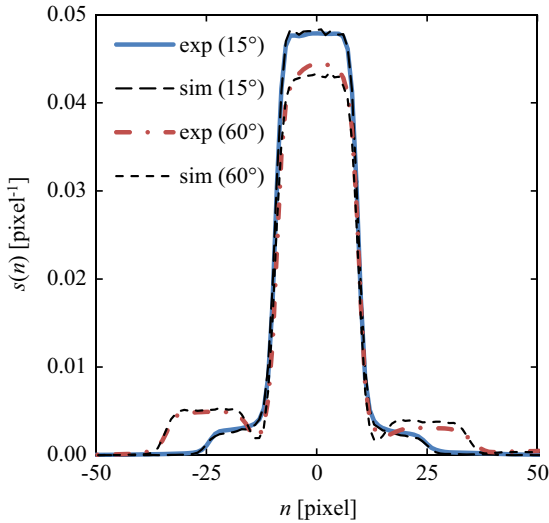

Fig. 11. AgGlass4 mm with the direction of perfect planarity perpendicular to the plane of incidence at 555 nm. Experimentally measured reflected beam profiles at $\theta = 15°$ (solid) and $\theta = 60°$ (dash-dotted), and numerically simulated beam profiles with $\theta_{n,x} = 0.17$ mrad, $\sigma = 0$ mrad (dashed).

space [7,41,42], which, for small scattering angles, stretches the scattering distribution in the plane of incidence by a factor of roughly $1/\cos\theta$. Based on purely geometric considerations for specular reflection from a surface with macroscopic slope errors, the scattering angle in the plane of incidence is twice the surface slope error independent of the incidence angle [40]. A simple description of incidence angle dependence that is straightforward to integrate in a MC program is obtained by a power law of $\cos\theta$. The trend lines and equations for the different materials and manufacturing directions are also indicated in Fig. 10.

4.4.3. Non-planarity of silvered glass

The scattering of AgGlass4 mm in Table 3 is reported for the direction of perfect planarity approximately parallel to the plane of incidence, i.e. a projected angle in the plane of incidence of zero between the surface normal vectors of the glass front and silvered back surfaces. The reflected beam profiles at 555 nm and incidence angles of 15° and 60° measured for the perpendicular material

orientation are shown in Fig. 11. In this direction, the main slit image is accompanied on either side by further images of the slit with lower intensity. This originates from a variation in glass thickness in x-direction, which causes a planarity error between the reflective silvered back surface and the front surface of the glass, denoted by $\theta_{n,x}$. Tracing a ray through refraction and reflection at a second surface reflector according to Snell's law [38] yields for the scattering angle $\theta_{s,x}$

$$\theta_{s,x} = 2\theta_{n,x}\left(1 - m\frac{\sqrt{(n_1/n_0)^2 - \sin^2\theta}}{\cos\theta}\right) + O\left(\theta_{n,x}^2\right) \qquad (15)$$

where n_0 and n_1 denote the indices of refraction of the surroundings and the glass, respectively, and m is the number of reflections at the back surface. For $m=0$ the ray is directly reflected from the front surface and the reflection error is twice the surface slope error (leftmost slit image in Fig. 11). For $m=1$, the slope error of the front glass surface is overcompensated by refraction, which corresponds to the main slit image. For $m > 1$ the scattering angle keeps increasing with the number of internal reflections (right slit images). By means of the distance between the slit images in Fig. 11 and Eq. (15), the surface normal error of the glass front surface is determined to be $\theta_{n,x} = 0.17$ mrad. This result is verified by MC ray-tracing where the back-silvered glass is modeled as described in Section 5 with a front-surface normal error of $\theta_{n,x} = 0.17$ mrad in the plane of incidence and $\sigma = 0$ mrad, i.e. perfect specular reflection at the back surface. The numerically simulated reflected beam profiles at 555 nm and incidence angles of 15° and 60° are also shown in Fig. 11. The good agreement at both incidence angles validates the optical modeling approach of the back-silvered glass and confirms the surface slope error of the front surface. Furthermore, since a good agreement with experiments is obtained for $\sigma = 0$ mrad in the MC simulations, it is likely that angular scattering with the direction of perfect planarity approximately parallel to the plane of incidence as reported in Table 3 is also caused by a small angular error of the front surface normal in that direction. This also explains the dependence on incidence angle as the scattering angle is scaled by the factor $\sqrt{(n_1/n_0)^2 - \sin^2\theta}/\cos\theta$, which increases with incidence angle from 1.55 at 15° to 2.5 at 60° (assuming $n_0=1$ for air and $n_1=1.518$ for N-BK7 glass at 555 nm).

5. Application to solar concentrators

In this section, the materials characterized in the previous two sections are employed in solar concentrators to elucidate the impact of the measured optical properties on the optical performance of the solar concentrator.

5.1. Optical modeling

5.1.1. Angular errors of solar concentrators

According to [40,43], the variance of the total angular error of a solar concentrator can be expressed as the sum of variances from different sources of error,

$$\sigma_{s,total}^2 = \sigma_{s,specularity}^2 + 4\sigma_{n,slope}^2 + 4\sigma_{n,shape}^2 + 4\sigma_{n,alignment}^2 + \sigma_{n,tracking}^2 \qquad (16)$$

where the standard deviations of surface normal errors (subscript n) are multiplied by a factor 2 to transfer from surface slope error to scattering angle (subscript s). For Fresnel reflectors that are actuated independently of the solar receiver, $\sigma_{n,tracking}$ is also multiplied by 2 [40]. In MC ray-tracing, all effects are conveniently simulated by a single, cumulative error of the surface normal with

standard deviation $\sigma_{n,total} = \sigma_{s,total}/2$ [44]. It is noted that the factor 2 between surface normal and reflection angle only holds in the plane of incidence ($\theta_{s,x} = 2\theta_{n,x}$), whereas in the plane perpendicular to the plane of incidence, the scattering angle is attenuated by the cosine factor of the incidence angle ($\theta_{s,y} = 2\theta_{n,y} \cos \theta$) [40]. Accordingly, simulating scattering due to non-specularity of the reflector material by a surface normal error generally yields non-conservative results. However, considering that all errors on the right-hand-side of Eq. (16), except for specularity, are described by macroscopic deviations of the surface normal, and that microscopic non-specularity is usually small compared to the other errors, this approach is considered appropriate for the simulation of solar concentrators.

5.1.2. Reflective materials

The solar reflective material is modeled as a specularly reflecting surface with measured $R_{specular,\lambda}$. Angular surface scattering is simulated by Gaussian surface slope errors in the two main directions of the material with the parameters given in Table 3 or [39] for materials that are better described by a superposition of two Gaussian distributions. Note that the reported standard deviations need to be divided by 2 to convert from scattering angle to surface slope error. In the case of a back-silvered glass reflector, the glass layer is included as a refractive, absorptive medium using spectral data of N-BK7HT [45] for the index of refraction and absorption coefficient. The silvered back surface is specularly reflecting with spectral surface reflectivity $\rho_{1,\lambda}$ calculated by

$$\rho_{1,\lambda} = \frac{R_{specular,\lambda} - \rho_{0,\lambda}}{(1 - (2 - R_{specular,\lambda})\rho_{0,\lambda})\tau_\lambda^2} \qquad (17)$$

where $\rho_{0,\lambda}$ is the spectral surface reflectivity of the front surface given by Fresnel's equations, τ_λ is the spectral internal transmissivity of the glass layer according to Bouguer's law with the angle of refraction calculated according to Snell's law, and $R_{specular,\lambda}$ is the measured spectral specular reflectance of the sample [38]. Eq. (17) guarantees that the simulated reflectance of the back-silvered glass matches the measured specular reflectance. To calculate the standard deviation of surface scattering at the silvered back-surface ($\sigma_{s,1}$) from the experimentally measured standard deviation ($\sigma_{s,0}$), refraction at the glass front surface according to Snell's law needs to be

Table 4
Material configurations for solar concentrators.

Configuration	Protective film	Solar reflector
Design 1	none	AgGlass4 mm
Design 2	none	AgFilm#1
Design 3	ETFE100 μm	AlFilm
Design 4	FEP100 μm	AgSheet#2

taken into account,

$$\sigma_{s,1} = \sigma_{s,0}\frac{\cos \theta}{\sqrt{(n_1/n_0)^2 - \sin^2\theta}} + O\left(\sigma_{s,0}^2\right) \qquad (18)$$

where n_1 and n_0 denote the indices of refraction of the glass and surrounding air, respectively. No angular deviation between the glass front surface and the silvered back surface is considered other than that resulting from curvature of the solar reflector (cf. Section 4.4).

5.1.3. Semi-transparent materials

Polymeric films are modeled as a refracting, absorbing, and narrow-angle scattering medium. The refractive index and absorption coefficient are determined from measured T_λ. Using a constant refractive index (1.37 for ETFE, 1.33 for FEP) and spectral data for the extinction coefficient determined from the measured normal transmittance spectrum, the measured T_λ is reproduced well at all incidence angles. Angular scattering is modeled as an isotropic Gaussian error of the transmitted ray direction within the refractive medium, with standard deviations calculated according to Eq. (18).

5.2. Concentrator design

Four different material configurations, listed in Table 4, are selected to build a solar concentrator: two designs using outdoor solar reflectors and two designs using indoor reflectors protected by a semi-transparent top film. The designs are applied to two solar concentrators: (1) a parabolic dish concentrator with a flat disk receiver; and (2) a parabolic trough concentrator with a circular tubular receiver. Geometric cross-sections of the parabolic dish and trough collectors are shown in Fig. 12a) and b), respectively. The rim angles Φ_{rim} of the solar concentrators are chosen for maximum theoretical geometric concentration. The geometric concentration ratios of a parabolic dish concentrator with a flat disk receiver and a parabolic trough concentrator with a circular tubular receiver are [46–48]

$$C_{g,dish} = \frac{\pi(a_i^2 - a_o^2)}{\pi a_o^2} = \left(\frac{\cos \Phi_{rim} \sin \Phi_{rim}}{\cos \theta_{acc} \sin \theta_{acc}}\right)^2 - 1 \qquad (19)$$

and

$$C_{g,trough} = \frac{2a_i}{2\pi r_o} = \frac{\sin \Phi_{rim}}{\pi \sin \theta_{acc}} \qquad (20)$$

respectively, where a_i is the inlet aperture half-width, a_o the outlet aperture half-width of the flat disk receiver, r_o the radius of the circular tubular receiver, and θ_{acc} the acceptance half-angle of the solar concentrator, as indicated in Fig. 12. Accordingly, $\Phi_{rim,dish} = 45°$ is chosen for the parabolic dish and $\Phi_{rim,trough} = 90°$ is chosen for the trough concentrator. The acceptance half-angle of the parabolic dish concentrator is set to $\theta_{acc,dish} = 17.5$ mrad, which corresponds to the acceptance half-angle of the detector used in the specular reflectance measurements. For the parabolic trough
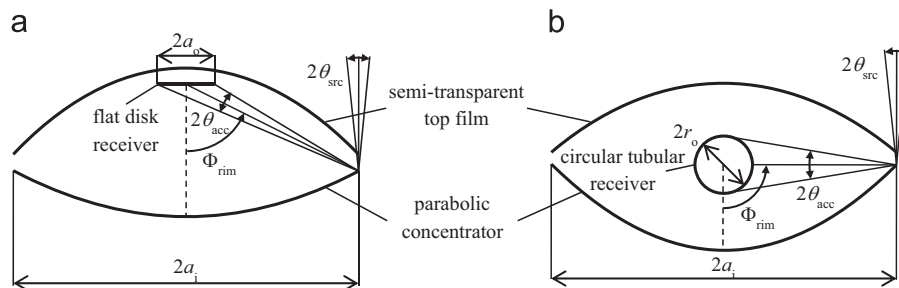

Fig. 12. Cross-sectional geometry of (a) a parabolic dish concentrator with a flat disk receiver and (b) a parabolic trough concentrator with a circular tubular receiver covered by a protective top film.
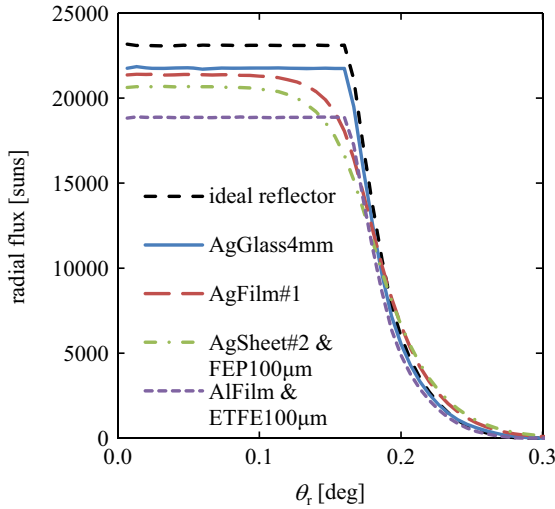
Fig. 13. Numerically simulated, circumferentially averaged solar flux distribution on the flat disk receiver of a parabolic dish collector as a function of the radial coordinate expressed in terms of the receiver acceptance angle for an ideal reflector and four different concentrator material configurations.
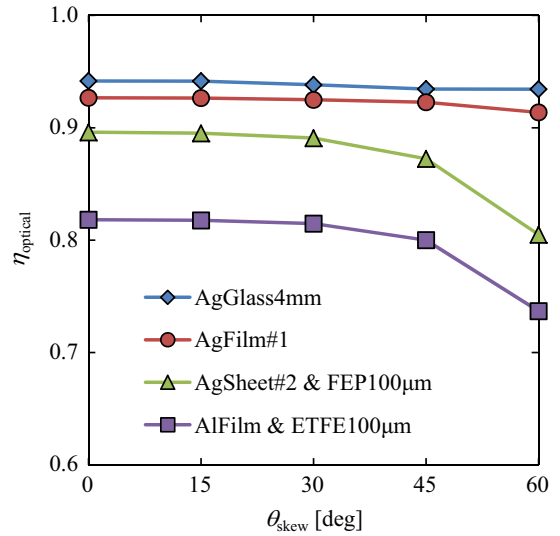

Fig. 14. Optical efficiency as a function of skew angle for a parabolic trough concentrator with a circular tubular receiver and four different material configurations.

The average solar concentration ratio is defined as

$$C = \frac{\Phi_{receiver}}{A_o E} = \cos \theta_{skew} \eta_{optical} C_g \qquad (22)$$

5.3. Results

5.3.1. Parabolic dish concentrator

The numerically simulated, circumferentially averaged solar flux distribution on the flat disk receiver as a function of the radial coordinate is shown in Fig. 13 for the four different material configurations and for an ideal parabolic dish concentrator with unity reflectivity and perfect specularity (reference). For convenience, the radial coordinate, which may be written from Eq. (19) as,

$$r = a_i \frac{\cos \theta_r \sin \theta_r}{\cos \Phi_{rim} \sin \Phi_{rim}} = a_i \frac{\sin 2\theta_r}{2 \cos \Phi_{rim} \sin \Phi_{rim}} \qquad (23)$$

is represented in Fig. 11 as the radial acceptance angle of the solar receiver,

$$\theta_r = \frac{1}{2} \arcsin\left(2 \cos \Phi_{rim} \sin \Phi_{rim} \frac{r}{a_i}\right)$$
$$\approx \frac{r}{a_i} \cos \Phi_{rim} \sin \Phi_{rim} \qquad (24)$$

For all material configurations, the concentrated solar radiation is absorbed within the design acceptance angle of 1°. Consequently, the intercept factor, defined as the ratio of solar radiation intercepted by the receiver aperture to the solar radiation reflected from the concentrator, is equal to 1 in all cases. Additionally, the flux distributions created by the highly specular materials (AgGlass4 mm, AlFilm) differ from the flux profile of an ideal reflector only in terms of the absolute value of solar concentration due to absorption, whereas the flux distribution shapes are nearly identical. Accordingly, angular scattering is negligible for these materials. The solar flux distributions of the less specular reflector materials, namely AgFilm#1 and AgSheet#2, show some angular dispersion at the edge of the distribution, indicating that angular scattering should be taken into account for these materials to accurately simulate the solar flux distribution on a receiver. The average solar concentration ratio (in suns) is 772 for AgGlass4 mm, 759 for AgFilm#1, 670 for AlFilm & ETFE100 μm, and 733 for AlSheet#2 & FEP100 μm, compared to the theoretical geometric concentration of 820 with an ideal reflector. The highly specular AlFilm potentially allows surpassing the average solar

concentrator, $\theta_{acc,trough} = 12.0$ mrad [49]. This acceptance angle applies at the rim where the distance to the focus is maximal. The corresponding angles calculated at the vertex and at the mean focus distance are 23.9 and 17.9 mrad, respectively. Accordingly, the detector acceptance angle used in the specular reflectance measurements closely resembles the average conditions in state-of-the-art parabolic trough concentrators. a_i is chosen in both cases as 3 m, which is in the range of current parabolic trough concentrators [49]. The semi-transparent top film, if present, is considered to form a convex shape of circular cross-section with radius of curvature of 8.4 m and 4.6 m for 100 μm films of ETFE and FEP, respectively.

The sun is modeled as a solar disk with a half-subtended angle of 4.65 mrad and spectral irradiance distribution according to the ASTM G173-03 AM 1.5 reference spectrum. Thus, the source divergence angle $\theta_{src} = 4.65$ mrad. The concentrator is assumed to be free of surface slope, shape, alignment and tracking errors to simulate the maximum attainable concentration with the different materials. For the parabolic trough concentrator, either the parabolic shape or an array of tangentially adjacent circular arc segments is applied [14], as the latter can reach the theoretical geometric concentration of a parabolic shape [48]. For the parabolic dish concentrator, optical properties measured at $\theta = 15°$ are used because θ varies between 0° and 22.5° and the measured reflective properties are generally weakly dependent on incidence angle. For the parabolic trough concentrator, properties measured at the skew angle, i.e. the incidence angle of sunrays on the concentrator inlet aperture $\theta = \theta_{skew}$, are used, where for 0° and 30° reflective data measured at 15° and interpolated data between 15° and 45° are used, respectively. The solar receiver is modeled as a blackbody absorber. The optical efficiency is defined as the solar radiative power absorbed by the solar receiver divided by the solar radiation incident on the inlet aperture of the solar concentrator,

$$\eta_{optical} = \frac{\Phi_{receiver}}{A_i E \cos \theta_{skew}} \qquad (21)$$

where A_i is the inlet aperture area of the concentrator, E the direct normal irradiance of the sun, and $\theta_{skew} = 0°$ for the parabolic dish.

concentration achieved by AgFilm#1 and AgSheet#2 at a given intercept factor.

5.3.2. Parabolic trough concentrator

The optical efficiency of the parabolic trough concentrator for the four different material configurations is shown in Fig. 14 as a function of the skew angle. Similar to the parabolic dish concentrator, the circular tubular receiver intercepts all rays reflected from the parabolic trough concentrator, i.e. an intercept factor of unity is achieved at all incidence angles. Solar concentrators comprising a semi-transparent top film and an indoor reflector material are generally outperformed by outdoor solar reflectors in terms of $\eta_{optical}$ particularly at large incidence angles, since the latter do not suffer from Fresnel losses. However, the protective environment created by the semi-transparent top film has some practical advantages such as no soiling of reflector/receiver, reduced material degradation, and reduced sensitivity to wind.

6. Conclusion

The optical properties of various materials for solar concentrators were measured over the solar spectrum and as a function of the incidence angle. The spectrally and directionally resolved values were used to determine the solar-weighted specular reflectance and narrow-angle transmittance, as well as the angular scattering. These were incorporated in Monte Carlo ray-tracing simulations to elucidate their effect in the optical performance of solar concentrators. It is found that the optical efficiency and the solar concentration ratio are strongly dependent on the reflectance and transmittance of materials, while the effect of non-specularity is secondary and affects rather the solar flux distribution. For a parabolic dish concentrator of 45° rim angle and ideal geometry, the highest solar concentration ratio is obtained for back-silvered glass, followed by silvered polymer film, silvered aluminum sheet covered by FEP film, and aluminized boPET film covered by ETFE film. For a parabolic trough concentrator of 90° rim angle and ideal geometry, the percentage decrease of optical efficiency with incident skew angle from 0° to 60° is 1% for outdoor reflectors and 10% for indoor reflectors protected by semi-transparent film covers.

Acknowledgments

References

[1] ASTM G173-03, Standard Tables for Reference Solar Spectral Irradiances: Direct Normal and Hemispherical on 37° Tilted Surface, 2012.

[2] S. Meyen, M. Montecchi, C. Kennedy, G. Zhu, M. Gray, J. Crawford, S. Hiemer, W. Platzer, A. Heimsath, M.O`Neill, S. Ziegler, S. Brändle, A. Fernandez, Parameters and method to evaluate the solar reflectance properties of reflector materials for concentrating solar power technology – Official reflectance guideline version 2.5, SolarPACES, June 2013.

[3] J.E. Proctor, P.Y. Barnes, NIST high accuracy reference reflectometer-spectrophotometer, J. Res. Natl. Inst. Stand. Technol. 101 (1996) 619–627.

[4] R.B. Pettit, Characterization of the reflected beam profile of solar mirror materials, Sol. Energy 19 (1977) 733–741.

[5] I. Susemihl, P. Schissel, Specular reflectance properties of silvered polymer materials, Sol. Energy Mater. 16 (1987) 403–421.

[6] P. Beckmann, A. Spizzichino, The Scattering of Electromagnetic Waves From Rough Surfaces, Artech House, Norwood MA, 1987.

[7] J.C. Stover, Optical Scattering: Measurement and Analysis, 2nd ed., SPIE optical engineering press, Bellingham WA, 1995.

[8] S. Schröder, A. Duparré, L. Coriand, A. Tünnermann, D.H. Penalver, J.E. Harvey, Modeling of light scattering in different regimes of surface roughness, Opt. Express 19 (2011) 9820–9835.

[9] A. Heimsath, T. Schmid, P. Nitz, Angle resolved specular reflectance measured with VLABS, Energy Proced. 69 (2015) 1895–1903.

[10] S. Meyen, F. Sutter, P. Heller, A. Oschepkov, A. New, Instrument for measuring the reflectance distribution function of solar reflector materials, Energy Proced. 49 (2014) 2145–2153.

[11] C.E. Kennedy, K. Terwilliger, Optical durability of candidate solar reflectors, J. Sol. Energy Eng. 127 (2005) 262–269.

[12] G. Jorgensen, R. Gee, M. DiGrazia, Development and Testing of Abrasion Resistant Hard Coats for Polymer Film Reflectors, In: SolarPACES, Perpignan, France, 2010.

[13] R. Bader, P. Haueter, A. Pedretti, A. Steinfeld, Optical design of a novel two-stage solar trough concentrator based on pneumatic polymeric structures, J. Sol. Energy Eng. 131 (2009) 031007.

[14] R. Bader, A. Pedretti, A. Steinfeld, A 9-m-aperture solar parabolic trough concentrator based on a multilayer polymer mirror membrane mounted on a concrete structure, J. Sol. Energy Eng. 133 (2011) 031016.

[15] P. Good, G. Zanganeh, G. Ambrosetti, M. Barbato, A. Pedretti, A. Steinfeld, Towards a commercial parabolic trough CSP system using air as heat transfer fluid, Energy Proced. 49 (2014) 381–385.

[16] B. Bierman, J. O'Donnell, R. Burke, M. McCormick, W. Lindsay, Construction of an enclosed trough EOR system in South Oman, Energy Proced. 49 (2014) 1756–1765.

[17] B. Bierman, C. Treynor, J. O'Donnell, M. Lawrence, M. Chandra, A. Farver, P. von Behrens, W. Lindsay, Performance of an enclosed trough EOR system in South Oman, Energy Proced. 49 (2014) 1269–1278.

[18] R.H. French, J.M. Rodríguez-Parada, M.K. Yang, R.A. Derryberry, N.T. Pfeiffenberger, Optical properties of polymeric materials for concentrator photovoltaic systems, Sol. Energy Mater. Sol. Cells 95 (2011) 2077–2086.

[19] ISO 9050, Glass in building – Determination of light transmittance, solar direct transmittance, total solar energy transmittance, ultraviolet transmittance and related glazing factors, 2014.

[20] Flabeg, Mirrors for CSP & CPV. ⟨http://www.flabeg-fe.com/en/solar/mirrors-for-csp-cpv.html⟩ (09.06.2015).

[21] 3M, 3M Solar Mirror Film 1100, Technical data sheet, January 2012.

[22] ReflecTech, ReflecTech Plus Mirror Film, Brochure, November 2011.

[23] Toray, Lumirror U50 – Technical Data Sheet. ⟨http://www.toraytpa.com/sites/default/files/data_sheets/LUM_PS-0017_U50-DATASHEET_METRIC.pdf⟩ (09.06.2015).

[24] Alanod Solar, Efficiency, solar, surfaces, Brochure, November 2014.

[25] Alanod, Miro-Silver, Brochure, November 2014.

[26] Almeco, Vega – Lighting applications, Brochure, November 2013.

[27] Almeco, Vega energy – Solar reflective surfaces, Brochure, January 2015.

[28] Toray Advanced Film, TOYOFLON – ETFE Properties. ⟨http://www.toray-taf.co.jp/en/product/pdf/2_013_1toyoflon_etfe.pdf⟩ (09.06.2015).

[29] Toray Advanced Film, TOYOFLON – FEP Properties. ⟨http://www.toray-taf.co.jp/en/product/pdf/2_013_1toyoflon_fep.pdf⟩ (09.06.2015).

[30] Schott, Borofloat 33 – Borosilicate glass. ⟨http://www.schott.com/borofloat/english/⟩ (09.06.2015).

[31] M. Zettl, High performance coatings for solar receivers and new dedicated manufacturing solution, Energy Proced. 48 (2014) 701–706.

[32] F.E. Nicodemus, J.C. Richmond, J.J. Hsia, I.W. Ginsberg, T. Limperis, Geometrical Considerations and Nomenclature for Reflectance, National Bureau of Standards, Washington D.C., 1977, October.

[33] ASTM E903-12, Standard Test Method for Solar Absorptance, Reflectance, and Transmittance of Materials Using Integrating Spheres, 2012.

[34] R. Siegel, J.R. Howell, Thermal Radiation Heat Transfer, 4th ed., Taylor & Francis, New York, 2002.

[35] P.S. Coray, W. Lipiński, A. Steinfeld, Spectroscopic goniometry system for determining thermal radiative properties of participating media, Exp. Heat. Transf. 24 (2011) 300–312.

[36] ISO 7668, Anodizing of aluminium and its alloys – Measurement of specular reflectance and specular gloss of anodic oxidation coatings at angles of 20 degrees, 45 degrees, 60 degrees or 85 degrees, 2011.

[37] A. Rabl, P. Bendt, Effect of circumsolar radiation on performance of focusing collectors, J. Sol. Energy Eng. 104 (1982) 237–250.

[38] M.F. Modest, Radiative Heat Transfer, 2nd ed., Academic Press, San Diego, 2003.

[39] P. Good, T. Cooper, M. Querci, N. Wiik, G. Ambrosetti, A. Steinfeld, Spectral data of specular reflectance, narrow-angle transmittance and angle-resolved surface scattering of materials for solar concentrators, Data in Brief, submitted.

[40] A. Rabl, Active Solar Collectors and Their Applications, Oxford University Press, New York, 1985.

[41] J.E. Harvey, Light-scattering Characteristics of Optical Surfaces (Ph.D. thesis), University of Arizona, United States, 1976.

[42] J.E. Harvey, Surface Scatter Phenomena: A Linear, Shift-Invariant Process, In: SPIE, 1989, pp. 87–99.

[43] T. Cooper, A. Steinfeld, Derivation of the angular dispersion error distribution of mirror surfaces for Monte Carlo ray-tracing applications, J. Sol. Energy Eng. 133 (2011) 044501.

[44] H. Lee, The geometric-optics relation between surface slope error and reflected ray error in solar concentrators, Sol. Energy 101 (2014) 299–307.

[45] Schott Advanced Optics, Optical glass, Catalogue, April 2015.

        P. Good et al. / Solar Energy Materials & Solar Cells 144 (2016) 509–522

[46] D.A. Harper, R.H. Hildebrand, R. Stiening, R. Winston, Heat trap: an optimized far infrared field optics system, Appl. Opt. 15 (1976) 53–60.

[47] R. Winston, J.C. Miñano, P. Benitez, Nonimaging Optics, Academic Press, United States, 2005.

[48] T. Cooper, M. Schmitz, P. Good, G. Ambrosetti, A. Pedretti, A. Steinfeld, Non-parabolic solar concentrators matching the parabola, Opt. Lett. 39 (2014) 4301.

[49] A. Fernandez-Garcia, E. Zarza, L. Valenzuela, M. Pérez, Parabolic-trough solar collectors and their applications, Renew. Sustain. Energy Rev. 14 (2010) 1695–1721.